

Wavefield characteristics and spatial incoherency - a comparative study from Argostoli rock- and soil-site dense seismic arrays

Afifa Imtiaz, Vincent Perron, Fabrice Hollender, Pierre-Yves Bard, Cécile Cornou, Angkeara Svay, Nikos Theodoulidis

▶ **To cite this version:**

Afifa Imtiaz, Vincent Perron, Fabrice Hollender, Pierre-Yves Bard, Cécile Cornou, et al.. Wavefield characteristics and spatial incoherency - a comparative study from Argostoli rock- and soil-site dense seismic arrays. Bulletin of the Seismological Society of America, 2018, 108 (5A), pp.2839-2853. 10.1785/0120180025 . cea-02339740

HAL Id: cea-02339740
https://cea.hal.science/cea-02339740

Submitted on 16 Mar 2020

HAL is a multi-disciplinary open access archive for the deposit and dissemination of scientific research documents, whether they are published or not. The documents may come from teaching and research institutions in France or abroad, or from public or private research centers.

L'archive ouverte pluridisciplinaire **HAL**, est destinée au dépôt et à la diffusion de documents scientifiques de niveau recherche, publiés ou non, émanant des établissements d'enseignement et de recherche français ou étrangers, des laboratoires publics ou privés.

Wavefield characteristics and spatial incoherency – a comparative study from Argostoli rock- and soil-site dense seismic arrays

by

A. Imtiaz[1,3], V. Perron[2,3,6], F. Hollender[2], P-Y. Bard[3], C. Cornou[3], A. Svay[4], N. Theodoulidis[5]

Corresponding Author:
Afifa Imtiaz
Bureau de Recherches Géologiques et Minières (BRGM)
Seismic and Volcanic Risks Unit
Risks and Prevention Division
3, Avenue Claude Guillemin - BP 36009 - 45060 Orléans cedex 2, France
Tel : +33(0)2 38 64 30 95
E-mail : a.imtiaz@brgm.fr
ORCID iD: https://orcid.org/0000-0001-6687-8690

(1) BRGM, F-45060 Orléans, France
(2) CEA, DEN, F-13108 St Paul lez Durance Cedex, France
(3) Univ. Grenoble Alpes, Univ. Savoie Mont-Blanc, CNRS, IRD, IFSTTAR, ISTerre, Bâtiment OSUG C, CS 40700, 38058 GRENOBLE Cedex 9, France
(4) IMSIA, University Paris-Saclay, France
(5) Institute of Engineering Seismology and Earthquake Engineering (ITSAK), GR-55102 Thessaloniki, Greece
(6) IRSN, F-92260 Fontenay-aux-Roses, France

ABSTRACT

The current article focuses on the results obtained from the analysis of seismic events recorded by a dense array located on a rock site at Argostoli in the Cephalonia Island of Greece. The objective of the study is threefold: (1) to explore to what extent the non-direct, diffracted surface waves influence the seismic wavefield at a rock site, (2) to investigate the loss of coherency of ground motions, and (3) to compare the results with those from a previously studied similar array located at an adjacent small, shallow sedimentary valley (soft-soil site). Both arrays consist of 21 velocimeters encompassing a central station in four concentric circles with diameters ranging from 10 to 180 m at the soft-soil and 20 to 360 m at the rock site. The seismic datasets under consideration include 40 or more events occurring around the site at epicentral distances up to 200 km having magnitudes ranging from 2 to 5. The seismic wavefields at both sites are analyzed by using the MUSIQUE algorithm: the backazimuth and slowness of the dominant incoming waves are extracted and the Love and Rayleigh waves are identified. Lagged coherency is estimated from the dataset, and the results are averaged for station pairs located at four separation distance intervals, 10–20, 20–30, 30–40 and 80–90 m. The results indicate that coherency at the rock site is, generally, larger than that from the soft-soil, especially at frequencies below 5 Hz. At soil site, lower coherency is observed for pairs along the valley-width direction while no such directional dependence is observed at the rock. The wavefield analysis shows that whilst about 40–60% of the seismogram energy at the soft-soil could be associated to diffracted surface waves (Love and Rayleigh) appearing mainly from the valley-width directions, only about 20% of energy at the rock site could be characterized as diffracted surface waves. Comparison with the widely-quoted parametric models reveals that the observed decay of coherency at both sites has little correlation with those from the models. These significant differences observed between the results of the rock and soil array indicate that the spatial incoherency is largely site dependent and is likely to be closely related with the formation of locally generated wavefield.

Keywords: Wavefield characteristics; Spatial Coherency; Dense Array; Rock Site; Soft-soil site; Cephalonia.

INTRODUCTION

The effects of spatial variability of earthquake ground motion (SVEGM), in other words the amplitude and phase variability of ground motion observed at two adjacent positions, have been of great interest for a long time in the design and analysis of large and extended structures. Though such variation is, generally, attributed to the wave passage delay, spatial incoherence and local site effects, the spatial incoherence caused by the effects of complex wave propagation and scattering has increasingly caught interest of the research community. It is a common practice to characterize the spatial phase variations by coherency functions from the stochastic analysis of dense seismic arrays. These functions represent the degree of correlation between ground motion measurements at two adjacent positions as an exponential decay with increasing frequency and interstation distance.

A great deal of existing literature into SVEGM has been devoted to the development of coherency models (see Zerva and Zervas 2002 and Liao 2006 for a review). However, the generalizability of these models remains uncertain due to the lack of their association with the physical site parameters. Much of the current literature is dedicated to the analysis of rather large dimension arrays (>100 m), located mostly at soil sites, and relevant for distances longer than the dimensions of most structures. Besides, complex wave propagation and scattering effects at rock-type ground conditions have received scant attention as the seismic wavefield is expected to be dominated by direct body waves at stiffer sites. As a result, there remains a paucity of research on the physical implications of short-distance spatial incoherency from rock-site dense arrays even though spatial incoherency has also been observed at rock sites owing to geological complexities such as weathering and shallow fracturation (Somerville et al. 1991; Steidl et al. 1996). In reality, horizontally extended structures (e.g., bridges) may be supported at different site conditions, soil or rock or a combination, and thus be exposed to

different degrees of differential motions. Therefore, extending our attention to rock sites alongside soil sites could be instrumental in understanding the SVEGM as well as evaluating the site specific risk of infrastructures. The present study attempts to contribute to this area of research by presenting the results obtained from the seismic events recorded at two nearby dense arrays, located at a rock and a soft-soil site, at Argostoli in the Cephalonia Island of Greece. It aims at investigating to what extent non-direct, diffracted surface waves contribute to the seismic wavefield at both sites, and at examining the site-dependence of the spatial variation. The part of the research concerning the soft-soil site is drawn from Imtiaz (2015) and Imtiaz et al. (2014, 2015, 2017a, b). Hence, this paper first provides a brief literature review of the rock-site coherency models, presents the dense array deployed at Argostoli rock site, focuses on the results obtained from the corresponding data analysis, and proceeds on their comparison with those from the soil site.

The two dense arrays consist of 21 broadband velocimeters, placed in four circles, at diameters 20 to 360 m (rock) and 10 to 160 m (soft-soil), centered on a reference station. Two sets of earthquakes (40 events for the rock and 46 for the soft-soil array), with local magnitudes M_L 2–5, occurring within an epicentral distance (R_{epi}) of 200 km, are utilized to estimate the apparent propagation characteristics of the waves and to identify the energies carried out by Love and Rayleigh waves. The 'lagged' coherency is calculated as a measure of random variability of the Fourier phase between any two stations in the array. Median coherency iss obtained for four separation distance intervals (10–20, 20–30, 30–40, and 80–90 m), common to both arrays, and compared with some widely-quoted coherency models developed for rock and soil sites.

COHERENCY FROM ROCK SITES

In current literature, very few coherency models are available for rock sites (e.g. Cranswick 1988; Menke et al. 1990; Toksoz et al. 1991; Abrahamson 2007). Schneider et al. (1992) compared coherency estimations from a set of rock- and soil-site arrays with the coherency function developed by Abrahamson et al. (1991) based on a soil site data (LSST, Taiwan array) for separation distance shorter than 100 m. The authors observed that the soil coherency fits well with the LSST model while the rock coherency seems comparable only when the site is not affected by topographic variations. Abrahamson (2007) studied the same set of arrays but removed the ones affected by the topographic variations. The author compared the respective average coherency from the soil, soft-rock and hard-rock sites, and observed a clear site dependence. At interstation distance 15–30 m, the coherency increases with the stiffness of the site. At 50–70 m, the soil and soft-rock estimates become comparable and the hard-rock remains higher. Zerva and Stephenson (2011) investigated seismic records from an array located on a variable site condition (valley and soft-rock) and observed that the complex wave propagation pattern affects not only the valley but also the surrounding soft-rock. The authors then highlighted the significance of irregular subsurface topography and formation of surface waves in the physical understanding of the spatial variation. Konakli et al. (2014) estimated coherency from the USGS Parkfield rock array for the 2004 Parkfield mainshock and compared with some existing models. Their result revealed that the observed variability of coherency decay rate, as a function of frequency and interstation distance, was not reproduced by the semi-analytical model of Luco and Wong (1986). At smaller interstation distances (<100 m), the estimates were lower than those from the empirical model of Ancheta et al. (2011), updated from Abrahamson et al. (1991), and the trend reverses at longer distances (>300 m). The authors concluded, once again, by indicating a rather complex dependence of coherency on effects related to source, propagation, topography and site, and the difficulty associated with

the task of explaining them by means of general, simplified processes. In a recent study, Svay et al. (2017) estimated plane-wave coherency from an another subset of data consisting of smaller magnitude (M_L 2.7-3.6), local events (R_{epi} 10-30 km) from the Argostoli rock array and observed that both the Luco and Wong (1986) and Abrahamson (2007) models do not provide a satisfactory match with estimated coherency values. A better fit is obtained when site-specific decay parameters are considered in the functional forms of the parametric models.

ARGOSTOLI DENSE SEISMIC ARRAYS

Located in the north-westernmost boundary of the Aegean plate, the Ionian Island of Cephalonia is considered to be one of the most active seismo-tectonic regions in Europe. The high seismicity of the area is associated with the dextral Cephalonia Transform Fault (CTF), situated in the northwestern boundary of the island (Figure 1a) and capable of generating earthquake magnitudes up to M = 7.4 (Louvari et al. 1999). The rate of seismic slip in the CTF is observed to be varying from 7 to 30 mm/yr (Anzidei et al. 1996; Hollenstein et al. 2006). Historical data show that more than 10 earthquakes of magnitudes between 6.5 and 7.5 occurred in the area between 1900 and 1998 causing major destruction. Two major earthquakes (moment magnitude Mw 6.1 and 6.0, and hypocentral depth ~10 km) hit the area on January 26 and February 3, 2014 (Karakostas et al. 2015; Theodoulidis et al. 2016). These events were associated with the CTF and occurred within 20 km distance of the Argostoli town, damaging a significant number of engineering structures. They were also followed by numerous aftershocks up to Mw 5.5. A post seismic campaign was conducted at Argostoli area (Figure 1a) within the framework of the SINAPS@ project, funded by the French Research Agency (ANR). A dense two-dimensional (2D) dense array, referred as “rock array” in this work (Figure 1b,c), intended to study short distance spatial variability of ground motion, was deployed on the rock formation from February 6 to March 10, 2014 (Perron et al. 2018). This

network complements the dataset recorded by a geometrically similar, smaller-size array, referred as “soft-soil array” here (Figure 1b,d), on the nearby small, shallow, sedimentary valley of Koutavos-Argostoli. The array was operational from September 2011 to April 2012 under the framework of EU-NERA (European Union - Network of European Research Infrastructures for Earthquake Risk Assessment and Mitigation) 2011–2014 project (Imtiaz 2015). The rock array was deployed on a Cretaceous massive limestone (karstified and fractured) formation located about 2 km southeast of the soft-soil array. Figure 1b displays the geological formation of the study area after Cushing et al. (2016). Geophysical surveys led to the determination of the V_{S30} (i.e., the harmonic mean of the shear-wave velocities over the 30 m of soil) as around 250 m/s for the soft-soil site, and 830 m/s for the rock site.

The rock array consists of 21 three-component (3C), broadband velocimeters (Güralp CMG6TD sensors with 30 s eigenperiods with integrated digitizers) belonging to different SINAPS@ partners (Perron et al. 2017). The stations are placed on the same geological unit, along four circles of diameters 20, 60, 180 and 360 m around the central station B0R0 (Figure 1c). On each circle, the stations branch off from B0R0 in N67°E, N139°E, N218°E, N286°E and N356°E directions. The signals are digitized at 200 samples per second; hence, the Nyquist frequency is 100 Hz. Figure 1d shows the configuration of the soft-soil array. This array also consists of 21 3C, broadband velocimeters (Güralp CMG40T sensors with eigenperiods between 30 and 60s) connected to Nanometrics Taurus digitizers, belonging to the French SISMOBRESIF national pool of portable seismic instruments. The stations are positioned in four concentric circles, with diameters 10, 30, 80 and 160 m, around the central station A00. Five stations, branching off from A00 in five directions, N39°E, N112°E, N183°E, N255°E and N328°E, are placed on each concentric circle. The resolvable frequency range for both the arrays could be considered as 1–20 Hz for slowness over 0.0004 s/m.

Both arrays provided a rich database by recording more than thousand earthquakes. The rock array recorded nearly 1850 good quality earthquakes with local magnitude ranging from 1 to 5, at epicentral distances up to 300 km, mainly corresponding to the seismic sequence of the aforementioned two consecutive earthquakes occurred in 2014, including some tens of events at greater distances and more varied azimuths (Hollender et al. 2015). A subset of 40 events with very good signal to noise ratio, local magnitude (M_L) 2 to 5, hypocentral depth (H) 4 to 40 km, epicentral distance (R_{epi}) 5 to 200 km, recorded by at least 20 stations of the array, is selected for the analysis. The events are chosen such that a homogeneous distribution of epicentral distance, magnitude and azimuthal coverage could be achieved, considering that most of the events occurred along the CTF in the west and some local M_L>3.5 events were saturated. The origin time, location and the magnitude of the events have been taken from the catalog of NOA (National Observatory of Athens) and Karakostas et al. (2015). The location of the selected events are presented in Figure 2a, and their characteristics are provided in Table 1. It is to be noted that in this study, the entire seismogram (duration beginning from the P-wave arrival up to the end of coda) is used for the wavefield analysis while the time window representing mainly the most energetic phase carried out by the S-wave is used for coherency estimation. Both durations are also given in Table 1. Figure 2b presents the durations of the selected events for coherency analysis as a function of respective hypocentral distances. A summary of the number of events grouped according to different parameters (distance, magnitude, backazimuth) is given in Table 2. Finally, the results from the analysis of rock array data are compared to those from a set of 46 events with similar characteristics (M_L 2-5 and R_{epi} up to 200 km) recorded by the soft-soil array. The details of this database is provided in Imtiaz (2015) and (Imtiaz et al. 2017b).

WAVEFIELD ANALYSIS

The MUSIQUE algorithm (Hobiger et al. 2012, 2016) is used to perform the wavefield characterization of the array data. MUSIQUE is a combination of the "classical" Multiple Signal Characterization (MUSIC) (Schmidt 1986; Goldstein and Archuleta 1987) and the quaternion-MUSIC (Miron et al. 2005, 2006) methods, that allows not only the extraction of backazimuth and apparent phase velocity (or slowness) of the dominant waves crossing the array but also their characterization as Love or Rayleigh waves. Detailed description of the MUSIQUE algorithm for 3C signals is available in Hobiger (2011) and Hobiger et al. (2016). Only a brief summary of the method is presented in the current article.

The basic principle of the method is to separate the signal and noise subspaces and then to estimate the signal parameters. Let us assume a dataset recorded by an array of N single-component sensors. As a first step, MUSIQUE calculates the cross-correlation matrix (in time domain) or cross spectral matrix (in frequency domain) for each frequency and time windows of interest, and defines the eigenstructure of the covariance matrix. The eigenvectors corresponding to the K strongest eigenvalues define the signal subspace (K<N) while the N-K weakest eigenvalues define the noise subspace. Then, from the set of array manifold vectors, the vectors that give the minimum projection onto the noise subspace are determined through the search of the maxima of the directional function (the so-called MUSIC spectrum). Once the signal vectors are determined, propagation direction and phase velocity of the dominant signals are computed as the functions of time and frequency. Quaternions, an extension of complex numbers into four dimensions (e.g. Ward 1997), are then used to characterize polarization parameters of an incident wave. The quaternion-MUSIC algorithm merges both the complex-valued data vectors of radial and vertical components into a single data matrix so that the phase information and the sense of rotation of the particle motion remains naturally preserved, hence,

allowing the distinction between retrograde and prograde Rayleigh wave motions. Although the classical MUSIC is able to identify multiple sources, the MUSIQUE code is presently limited to a single wave contribution, i.e. to the most dominant source (K=1) as it requires projecting the horizontal signals with respect to the identified wave backazimuth in order to estimate the polarization parameters.

As a first step of the data analysis, the entire length of signal is divided into smaller sub-windows of five periods as a function of frequency. Here 200 log-based steps between 1 to 20 Hz frequency are used and the sub-windows are overlapped by 50%. A spectral averaging is done over five frequency samples centered on each frequency step in order to assure a well-conditioned covariance matrix. Then the slowness and backazimuth (θ) of the most dominant incident wave for each sub-window of the signal is determined from the MUSIC spectrum. The radial and transverse components are computed by projecting the east-west (EW) and north-south (NS) components of the signals along the identified backazimuth (θ) and its orthogonal direction. During the post-processing, the results from the sub-windows containing energy less than the median energy of all the analyzed windows of an event are filtered out. Additionally, the sub-windows having signal to noise ratio less than 5 and slowness outside the range of 0.0004 to 0.008 s/m (apparent velocity 125 m/s to 2500 m/s) are also filtered out. A detailed description of the post-processing calculations is given in Imtiaz (2015).

Figure 3 shows EW component of the velocity time series of an M_L=3.5 earthquake (ID # 11 in Table 1) recorded by all the stations of the rock array. The event occurred at a hypocentral deth (H) of 31 km, an epicentral distance (R_{epi}) 13 km and, and a backazimuth (θ) N348°E. Figure 4a illustrates the retrieved backazimuths of the dominant incident waves from all the analyzed sub-windows as a function of time. The colorbar corresponds to the ‘normalized

energy' of the respective windows, defined as the energy carried out by the sub-window divided by the squared Fourier amplitude. On this plot, the P and S wave arrivals and their respective durations could be followed through the energy concentration of the results. It can also be observed that the energetic incident waves are not necessarily arriving from the source direction (N348°E, marked by the red horizontal line); they are rather scattered along other directions even in the earlier part of the seismogram (<10 s). Figure 4b presents the 2D histogram of backazimuth distribution as a function of frequency. In order to group the results, 72 grid points have been considered between N0°E and N360°E angles (interval = 5°) for the backazimuth axis and 31 log-based grid points between 1 and 20 Hz for the frequency axis. The colorbar indicates the summed 'normalized energy' of the analyzed sub-windows falling into the backazimuth-frequency grids. The histogram demonstrates that most of the energetic waves at frequencies lower than ~6 Hz are appearing from north to north-east (roughly N330°E to N30°E), which corresponds mainly to the event's backazimuth direction. The scattered energetic waves are observed at higher frequencies (>6 Hz).

Decomposition of diffracted surface waves

Next, the results corresponding to the direct arrivals (considered as waves coming from backazimuth ± 20° direction) are eliminated for each event in order to separate the diffracted wavefield and the estimates from all the individual events are summed. During the wavefield analysis, the dominant incident waves are identified as Love or Rayleigh waves based on the energy content of the analyzed signal window. A sub-window is characterized as Love- or Rayleigh-dominant, respectively, when the estimated transverse energy or the summation of the radial and vertical energy is more than 70% of the total energy of that window. If none of these criteria is fulfilled, no wave is identified for the sub-window under consideration. In order to summarize the observations from all the events and to focus on the surface wave composition, only the results corresponding to the windows 'identified' as Love or Rayleigh

275 are considered for further analysis. Hence, the ‘non-identified’ windows are also subtracted in
276 the process.
277
278 Figure 5a shows the summary of the backazimuth distribution of the entire diffracted wavefield
279 (waves ‘identified’ as Love and Rayleigh + waves remained ‘unidentified’) from all the 40
280 events recorded by rock array. Same as Figure 4b, 72 grid points have been considered between
281 N0°E and N360°E angles (interval = 5°) for the backazimuth axis and 31 log-based grid points
282 between 1 and 20 Hz for the frequency axis. The colorbar indicates the summed ‘normalized
283 energy’ of all the sub-windows from the dataset falling into the backazimuth-frequency grids.
284 It seems that the diffracted waves are arriving approximately from the north-south direction
285 over the entire frequency range for the rock array. The summary of the diffracted waves
286 identified as Love and Rayleigh is presented in Figure 5b and Figure 5c, respectively. While a
287 weak dominance of Rayleigh waves arriving from the north-south direction is evident at higher
288 frequencies (>5 Hz), an even weaker dominance of Love waves from the north-east is observed
289 at lower frequencies (<5 Hz). On the contrary, the similar results of the wavefield analysis
290 from the soft-soil array (Imtiaz et al. 2014) presented in Figure 5d-e show the predominance of
291 significant diffracted surface waves, propagating along SW-NE direction (Figure 5d), beyond
292 the fundamental frequency (~1.5 Hz) of the valley. The lower frequencies (1-3 Hz) seem to be
293 dominated by Love waves (Figure 5e) while the higher frequencies by both Love and Rayleigh
294 waves (Figure 5f).
295
296 Figure 6a-d illustrate the arithmetic mean ±1σ of diffracted and direct, Rayleigh and Love
297 energy as a percentage of the ‘total analyzed energy’ (all direct and diffracted waves) for the
298 rock and soft-soil array. On an average, about 20% of the ‘total analyzed energy’ from the rock
299 array could be characterized as diffracted Love and Rayleigh waves (Figure 6a). Love wave

composition seems to be slightly higher than Rayleigh only up to ~2 Hz frequency. In case of the soft-soil array (Figure 6b), the wavefield is found to be composed of a much higher proportion of surface waves, average ranging from 40% to 60%, over the entire analyzed frequency range. A clear frequency dependence of the energy distribution is also observed: lower frequencies (1–2.5 Hz) are dominated by Love waves, while certain narrow bands of higher frequencies are dominated either by Love or Rayleigh waves. Correlatively, only up to 5% and 5–10% of the 'total analyzed energy' could be characterized as direct surface waves for the rock and soft-soil arrays, respectively (Figure 6c,d). At both sites, more than 80% of the mean surface wave energy (Love + Rayleigh) correspond to the diffracted waves while only around 20% to the direct waves (Imtiaz 2015; Sbaa et al. 2017).

COHERENCY ANALYSIS

Estimation of lagged coherency

Coherency is a complex-valued function and characterizes the variation in Fourier phases between two ground motions. By definition, lagged coherency is supposed to remove the effects of systematic variation coming from the time delay in wave arrivals, known as the 'wave-passage effect'. Therefore, the two time histories under consideration are aligned using the time lag that leads to the largest correlation of the motions. In this study, the records from each station in the array are aligned with respect to the central station (B0R0 for the rock and A00 for the soil array). However, no remarkable time lag (generally <2% of the coherency window) is observed for both arrays. The duration of the most energetic, S-wave dominated signal window is selected for coherency analysis by visually inspecting the records of the central station. Details of the time-window selection procedure and the coherency estimation are provided in Imtiaz et al. 2017 (a, b).

The selected time windows of the signals are cut and tapered by using 5% cosine bell window at both ends. The cross- and auto-spectra of the motions are calculated and averaged over 11 frequency points by using a Hamming (M=5) window. Finally, the lagged coherency between a pair of stations is estimated as the modulus of the complex coherency, i.e., the ratio between the smoothed cross spectrum ($\bar{S}_{jk}$) of the pair of stations (j, k), normalized by the geometric mean of the smoothed power spectra at the respective stations ($\bar{S}_{jj}, \bar{S}_{kk}$), as function of the interstation distance (ξ) and frequency (1 to 25 Hz), and given by,

$$|\bar{\gamma}_{jk}(\xi, f)| = \frac{|\bar{S}_{jk}(f)|}{|\sqrt{\bar{S}_{jj}(f)\bar{S}_{kk}(f)}|} \quad (1)$$

The values of lagged coherency range from 0 to 1 for fully uncorrelated to fully correlated motions. When the interstation distance or frequency tends to zero the estimates tend to 1. Theoretically, at higher frequencies and larger interstation distances coherency tends to zero. However, in actual calculations the modulus of the complex coherency tends to a constant value significantly larger than zero due to the level of smoothing applied to the inherent noise in the data. The median value of this constant is considered as 0.33 when an 11-point Hamming window is applied for frequency smoothing (Abrahamson 1992). As the coherency estimates below this value are uninterpretable, it is termed as the 'resolvability threshold' in this article.

The lagged coherency estimated from the EW component of the velocity seismograms (Figure 3) of the event no.11 is shown in Figure 7a-d. The station pairs consist of the central station and the other stations located along the five array-branch directions (N 356, N 67, N 139, N 213 and N 286) on the concentric circles. For example, the station pairs considered in the Figure 7a are B0R0-B1R1, B0R0-B2R1, B0R0-B3R1, B0R0-B4R1 and B0R0-B5R1 (Figure 1c). Thus the four interstation or separation distances considered in Figure 7 correspond to the radii

of the concentric circles in the array, 10, 30, 90 and 180 m. As expected, the coherency is observed to decay with increasing frequency and separation distance. No clear variation is observed along the different direction of the pairs at a certain separation distance.

Median from the dataset

As the variability of coherency estimates is skewed, it is preferable to perform the statistical analysis on the ATANH (or, $\tanh^{-1}$) transformation in order to produce approximately normally distributed data (Harichandran 1991; Abrahamson et al. 1991). The 'median resolvability threshold' of lagged ATANH coherency is 0.34 when 11-point Hamming window is applied (Abrahamson 1992).

Coherency analysis from the soft-soil array (Imtiaz et al. 2017b) showed that when the median coherency is derived by averaging all station pairs irrespective of their orientations, the two geometric horizontal components (EW, NS) as well as their rotation along any physical direction result in almost similar estimates. The authors also suggested that the source related parameters had negligible effect on the loss of coherency of the dataset. Therefore, the horizontal components of the ground motion are not rotated and simply the EW and NS components are considered for presenting the results. Lagged coherency of the three components from all the available pairs of stations (max. 210 pairs per event) is estimated for the entire dataset. Table 3 shows the number of 'ideally available' (assuming data from all the 21 stations in the array are available) pairs of stations per event for the groups of separation distances between 10 and 100 m. Four separation distance ranges (10–20, 20–30, 30–40 and 80–90 m) that include maximum number of pairs from both arrays have been chosen to present the results. Median of the coherency estimates from the pairs available at a given distance range for a single event is defined as the 'individual median'. Then the 'global median' of the entire dataset at that given separation distance range is derived by combining all the available pairs

374 from all the events. Table 4 shows the number of total pairs considered from the entire dataset
375 for the estimation of 'global median' coherency.
376
377 The average coherency estimates from the rock array in terms of the 'individual median' of
378 each event (thin black curves) along with the 'global median' (thick black curve) of all events,
379 as a function of frequency, are presented in Figure 8a-d for the EW component and in Figure
380 8e-h for Z (vertical) components. The corresponding 'global median' from the soft-soil array
381 is also plotted in thick red curve. The measure of variability or standard deviation (σ) about the
382 respective 'global median' curve is also provided by dashed lines. Here the σ is calculated in
383 terms of Median Absolute Deviation (MAD), defined as the median of the absolute deviations
384 (i.e., residuals) about the median of the observations (see Huber 1981; Imtiaz et al. 2017b). A
385 logarithmic scale is used for the frequency axis to highlight the results that are less affected by
386 the resolvability threshold. However, the estimated median curves are observed to be well
387 above the threshold. The coherency seems to be larger on rock than on the soil, at least up to
388 5 Hz for the EW and 10 Hz for the Z components, and at all separation distances.
389
390 A directional variation of coherency estimates, depending on the orientation of the station-
391 pairs, was observed in the results from the soft-soil array (Imtiaz et al. 2017b). Therefore,
392 median coherency estimates from the horizontal components of the arrays are compared, by
393 grouping the pairs lying in five array-branch directions at different separation distances. The
394 results from the EW component are shown in Figure 9a-d for the rock array and in Figure 9e-
395 h for the soft-soil array. In case of the soft-soil array, a consistent directional dependence of
396 coherency is observed at all separation distances, the highest coherency being in the N 328 and
397 the lowest in the N 255 directions corresponding to the valley-parallel and -perpendicular axes,

398 respectively (Imtiaz et al. 2017b). However, no remarkable orientation dependence of
399 coherency is observed for the rock array.

400 **COMPARISON WITH EXISTING PARAMETRIC MODELS**

401 ***Selected parametric models***

402 A great variety of functional forms of lagged coherency is available in the literature although
403 very few are based on rock data. Some widely quoted parametric models are selected in this
404 article in order to compare with the median estimates from Argostoli data. Two semi-empirical
405 and two empirical models, applicable for short interstation distances (<100 m), pertinent to soil
406 and rock sites, are chosen and briefly presented below:

407

408 (a) The semi-empirical model of Luco and Wong (1986): It is based on the analysis of shear
409 waves propagating through a random medium and expressed as a double exponential decay
410 function of interstation distance (ξ) in m and angular frequency (ω) in rad/sec,

411 $$|\gamma(\xi,\omega)| = \exp(-\alpha^2\omega^2\xi^2) \quad (2)$$

412 The coherency drop parameter is given by $\alpha = \nu/V_s$, where V_s is the average shear-wave
413 velocity of the medium along the wave travel-path and ν is a constant related to the medium
414 properties. Typical values of α are suggested within 2×10^{-4} to 3×10^{-4} sec/m. In this study, rather
415 than estimating α from the dataset, the median value 2.5×10^{-4} sec/m is taken.

416

417 (b) The semi-empirical model of Menke et al. (1990): It is one of the very few rock site
418 coherency models available in the existing literature, expressed as an exponentially decaying
419 function of separation distance (ξ) in m and frequency (f) in Hz,

420 $$|\gamma(\xi,f)| = \exp(-\alpha f\xi) \quad (3)$$

where, α value is proposed within the range of 4×10^{-4} to 7×10^{-4} sec/m. Again, the he median value of α = 5.5 × 10-4 sec/m is considered in this study. The functional form of this model is almost similar to that of Luco and Wong (1986) except that the latter expresses a squared exponential decay of coherency. The Menke et al. (1990) model is seemingly the square root of the Luco and Wong. Hence, the Luco and Wong model shows a larger decrease at higher frequencies and larger separation distance, but the decay starts relatively later as "alpha" coefficient is smaller.

(c) The empirical model of Abrahamson (2007): Abrahamson proposed a purely empirical plane-wave coherency model for rock sites based on 78 earthquakes recorded at the Pinyon Flat array, which is expressed as,

$$|\gamma^{pw}(\xi, f)| = \left[1 + \left(\frac{f \tanh(a_1 \xi)}{f_c(\xi)}\right)^{n_1(\xi)}\right]^{-1/2} \left[1 + \left(\frac{f \tanh(a_1 \xi)}{a_2}\right)^{n_2}\right]^{-1/2} \quad (4)$$

The coefficients are given as:

a_1=0.4, a_2=40, $n_1(\xi)$=3.8-0.04ln(ξ+1)+0.0105[ln(ξ+1)-3.6]^2, n_2=16.4 and f_c=27.9-4.82 ln(ξ+1)+1.24[ln(ξ+1)-3.6]^2 for the horizontal component; and

a_1=0.4, a_2=200, $n_1(\xi)$=2.03+0.41ln(ξ+1)-0.078[ln(ξ+1)-3.6]^2, n_2=10 and f_c=29.2-5.20 ln(ξ+1)+1.45[ln(ξ+1)-3.6]^2 for the vertical component.

The plane-wave coherency is calculated by taking the real part of the smoothed cross-spectrum after aligning the ground motions on the best plane-wave speed. As such, it includes the random variations in the wave passage effect and should be lower than the lagged coherency, especially at higher frequencies and longer interstation distances.

(d) The empirical model of Ancheta et al. (2011) : Abrahamson et al. (1991) proposed an empirical model based on the estimation of lagged coherency from 15 earthquakes recorded at

a small array (LSST) located at a soil site in Lotung, Taiwan. This model allows investigations of coherency for the horizontal components of the ground motion and for station separation distance smaller than 100 m. Ancheta et al. (2011) proposed a slight modification in the first term of this model, by comparing an analysis from a set of events recorded by the Borrego Valley differential array (BVDA) located on an alluvium site, in order to correct the negative bias at separation distance ("ξ") smaller than 30 m. The resulting model is described as,

$$|\gamma(\xi,f)|=\tanh\{(3.79-0.499\ln(\xi))\left[\exp\{(-0.115-0.00084\xi)f\}+\frac{f^{0.878}}{3}\right]+0.35\} \quad (5)$$

Observation vs the selected parametric models

The estimated median coherency from the Argostoli rock and soft-soil arrays are compared at four separation distances with the aforementioned parametric models, and are illustrated in Figure 10a-d for the horizontal and in Figure 10e-h for the vertical component. Here the horizontal coherency is the arithmetic mean of the EW and NS component estimates. Instead of using the ATANH transformation, the results are presented in terms of coherency ($|\gamma|$) in order to facilitate the interpretation. The models are computed for distances 15, 25, 35 and 85 m. Note that the semi-empirical (Luco and Wong 1986; Menke et al. 1990) and empirical plane-wave (Abrahamson 2007) coherency models approach zero while the lagged coherency estimates from the data and the empirical model (Ancheta et al. 2011) tend to the resolvability threshold at higher frequencies. Thus, they are not comparable at those frequencies.

The rock coherency seems to be in fair agreement with the models over all the frequencies at 10–20 m, and up to 3 Hz frequency at other distances. As interstation distance increases, the models tend to overestimate the actual observations. The coherency values are always overestimated by the Abrahamson's hard-rock model. This may be due to the fact that the Argostoli rock array is situated on a lightly softer formation (V_{s30}=830 m/s) compared to the

data the model is based on (V_{s30}=1030 m/s). However, the soil-site model of Ancheta et al. (2011) also overestimates the rock array coherency at all the distances above 20 m.

One fundamental issue with the semi-empirical models is that they consider a constant decay rate with the wavelength whereas the real data exhibit varying decay tendencies with respect to frequency and interstation distance. Therefore, the double exponential decay of Luco and Wong (1986) model is observed to fit very well with the rock estimates at 80–90 m (up to about 6 Hz frequency) but not at shorter interstation distances. At shorter distances, coherency from the Argostoli data are observed to decay much faster compared with the semi-empirical models. This issue is somewhat taken care of by the empirical models but the overall decay rate in the data still remains faster than the models. Coherency estimates from the Argostoli soil array seems to be relatively poorly predicted by all the models. At shorter interstation distances (up to 40 m) and higher frequencies (>5 Hz) the observed rock coherency is, surprisingly, slightly lower than the soil. This could be attributed to the soil heterogeneities associated with the rock site (karst filled with decalcification clay, fractured zone) whose characteristic "wavelength" of variation is rather weak (metric to decametric).

Similar conclusions could be drawn for rock array data in case of the vertical component (Figure 10e-h). However, the vertical coherency from soil array seems to be decaying at a much faster rate up to about 7–8 Hz and shows a reverse tendency afterwards, especially at shorter interstation distances (10–40 m). This increasing trend is totally absent in the rock data. A possible explanation could be that the vertical coherencies at the soil site might be increased at some higher frequencies because of the presence of converted S-P waves or Rayleigh waves with higher phase velocities.

DISCUSSION AND CONCLUSIONS

The current study performs a twin analysis of wavefield characterization and spatial incoherency of seismic motion recorded at two dense arrays of stations, one located on a rock site, the other on a soft-soil site. As for the rock array, a large number (40) of small to moderate, shallow, local and regional events with relatively even distribution in magnitude, distance and backazimuth around the site, are analyzed. The loss of coherency is estimated for interstation distance ranging from 10 to 360 m. The median of the estimates at different interstation distance ranges (<100 m) have been examined and compared with those estimated from a similar dataset recorded at a nearby soil site as well as with some of the existing parametric models. The key results derived from the first part of the work, that is, the analysis of the wavefield composition, reveal that some wave scattering over the frequency range of 1–20 Hz is arriving from the north-south and north-east directions of the rock site for almost all the events. However, only 20% of the total seismogram energy could be associated to diffracted surface waves (Love and Rayleigh). As for the soft-soil array, about 40–60% of the analyzed seismogram energy could be characterized as diffracted surface waves associated to 2D or 3D geometrical effects, appearing mainly from the valley-width directions, with clear frequency-dependent dominance of Love and Rayleigh waves (Imtiaz et al. 2014). Besides, more than 80% of the total surface wave energy is observed to be carried out by the diffracted waves at both sites. Hence, it is evident that the formation of diffracted surface waves is much more significant, especially on the sedimentary valley (soft-soil site) compared to the rock site, and may play an important role in causing the higher loss of coherency and its directional variability.

In the second part of the work, the estimated median lagged coherency from the rock data exhibits very similar decaying tendencies for all the three components (EW, NS and Z). The

coherency is also found to be, generally, higher than that from the nearby soil site. However, at shorter interstation distances and higher frequencies, rock coherency seems to be slightly lower than that of soil. This could likely be attributed to the karstic-type weathering of the Cretaceous limestone of the investigated rock site. This weathering shows strong lateral lithological variation, with alternation at metric to decametric scale, of massive outcropping limestone areas with zones dominated by decalcifying clay content. Further investigation is suggested to better quantify this observation. The directional variability of lagged coherency, depending on the orientation of the station pairs, observed at the soft-soil site appears to be negligible for the rock site. Unlike the soft-soil site, coherency from vertical component seems to be comparable with the horizontal at the rock site. Comparison of the median coherency estimated from the arrays with the empirical models does not show any consistent correlation. Overall, the rock coherency is overestimated by all the parametric models even by the empirical one based on the soil data. Apparently, the decay rate of lagged coherency, as a function of frequency, seems to be not only site dependent but also interstation distance dependent. The fastest decay rate from the Argostoli data (both soft-soil and rock sites) is not well-captured by the empirical models. On the other hand, the variability in the decay rate, especially with respect to the interstation distance, is not addressed by the semi-empirical models. The findings of the present work reaffirm the site dependent nature of spatial variation and emphasize the need for more rigorous efforts on studying different sites in order to better understand the spatial variability of ground motion.

DATA AND RESSOURCES

The data used in the present work are open. The data from the rock and soft-soil sites can be obtained on the data repositories detailed in Perron et al. (2017) and Theodoulidis et al. (2017), respectively.

ACKNOWLEDGEMENTS

This work was carried out under the SINAPS@ project that receives French funding managed by the National Research Agency under the program “Future Investments” (SINAPS@ reference: ANR-11-RSNR-0022). SINAPS@ is a “Seism Institute” project (http://www.institut-seism.fr/en/). We would like to thank all the contributors of this work, especially for helping on the field during the SINAPS@ post-seismic campaign, Régis Cottereau (ECP), Marc Cushing (IRSN), Alberto Frau (CEA/EMSI), Sébastien Hok (IRSN), Philippe Langlaude (CEREMA), Aurore Laurendeau (CEA/LDG), Armand Mariscal (ISTerre) and Alexandros Savvaidis (EPPO-ITSAK), as well as our local help on the Cephalonia Island, Agis Konidaris (TEI) and Chrisostomos Andreou.

554 **REFERENCES**

555 Abrahamson NA (2007) Program on Technology Innovation: Effects of Spatial Incoherence
556 on Seismic Ground Motions. Rpt. No. EPRI 1015110, Palo Alto, CA

557 Abrahamson NA (1992) Spatial Variation of Earthquake Ground Motion for Application to
558 Soil-Structure Interaction. Rpt. No. EPRI TR-100463, Tier 1, Palo Alto, CA

559 Abrahamson NA, Schneider JF, Stepp JC (1991) Empirical Spatial Coherency Functions for
560 Application to Soil-Structure Interaction Analyses. Earthq Spectra 7:1–27. doi:
561 10.1193/1.1585610

562 Ancheta TD, Stewart JP, Abrahamson NA (2011) Effects of Surface Geology on Seismic
563 Motion. In: 4th IASPEI / IAEE International Symposium, University of California Santa
564 Barbara. California,

565 Anzidei M, Baldi P, Casula G, et al (1996) Repeated GPS surveys across the Ionian Sea:
566 evidence of crustal deformations. Geophys J Int 127:257–267. doi:
567 https://doi.org/10.1111/j.1365-246X.1996.tb04718.x

568 Cranswick E (1988) The information content of high-frequency seismograms and the near-
569 surface geologic structure of "hard rock" recording sites. Pure Appl Geophys PAGEOPH
570 128:333–363. doi: 10.1007/BF01772604

571 Cushing EM, Hollender F, Guyonnet-Benaize C, et al (2016) Close to the lair of Odysseus
572 Cyclops : the SINAPS@ postseismic campaign and accelerometric network installation
573 on Kefalonia island – Site effectcharacterizationexperiment. In: McCalpin J, Gruetzner C
574 (eds) Proceedings of the 7th INQUA on Paleoseismology, Active Tectonics and
575 Archeoseismology , Crestone, Colorado, USA, 30 May - 3 June.

576 Goldstein P, Archuleta RJ (1987) Array analysis of seismic signals. Geophys Res Lett I4:13–
577 16.

578 Harichandran RS (1991) Estimating the spatial variation of earthquake ground motion from

579 dense array recordings. Struct Saf 10:219–233.
580 Hobiger M (2011) Polarization of surface waves : characterization, inversion and application
581 to seismic hazard assessment. Université de Grenoble
582 Hobiger M, Cornou C, Bard P-Y, et al (2016) Analysis of seismic waves crossing the Santa
583 Clara Valley using the three-component MUSIQUE array algorithm. Geophys J Int
584 207:439–456. doi: 10.1093/gji/ggw289
585 Hobiger M, Le Bihan N, Cornou C, Bard P-Y (2012) Multicomponent Signal Processing for
586 Rayleigh Wave Ellipticity Estimation Application to Seismic Hazard Assessment. IEEE
587 Signal Process Mag 29:29–39–29–39.
588 Hollender F, Perron V, Imtiaz A, et al (2015) Close to the lair of Odysseus Cyclops : the
589 SINAPS@ postseismic campaign and accelerometric network installation on Kefalonia
590 Island. In: Proceedings of the 9th Colloque National AFPS 2015, Marne-La-Vallée,
591 France, 30 November - 2 December.
592 Hollenstein C, Geiger A, Kahle H-G, Veis G (2006) CGPS timeseries and trajectories of crustal
593 motion along theWest Hellenic Arc. Geophys J Int 164:182–191. doi:
594 https://doi.org/10.1111/j.1365-246X.2005.02804.x
595 Huber P (1981) Robust statistics. New York: John Wiley
596 Imtiaz A (2015) Seismic wave field, spatial variability and coherency of ground motion over
597 short distances : near source and alluvial valley effects. PhD Thesis. Université Grenoble
598 Alpes, English. <NNT : 2015GREAU002>. <tel-01148138>. https://tel.archives-
599 ouvertes.fr/tel-01148138
600 Imtiaz A, Cornou C, Bard P-Y (2017a) Sensitivity of Ground Motion Coherency to the Choice
601 of Time Windows from the Argostoli Dense Seismic Array. Bull Earthq Eng (under Rev
602 0:1–30.
603 Imtiaz A, Cornou C, Bard P-Y, Hobiger M (2014) Diffracted Wave Field And Coherency

Analysis: An Example From Dense Array Network In Argostoli Basin, Cephalonia, Greece. In: Proceedings of the Second European Conference on Earthquake Engineering and Seismology (2ECEES), Istanbul, Turkey, 24-29 August. p 12, Paper # 2351

Imtiaz A, Cornou C, Bard P-Y, Zerva A (2017b) Effects of site geometry on short-distance spatial coherency in Argostoli, Greece. Bull Earthq Eng 1–35. doi: https://doi.org/10.1007/s10518-017-0270-z

Imtiaz A, Cornou C, Bard P-Y, Zerva A (2015) Spatial coherence of seismic ground motion and geometric structure of the sub-surface: an example in Argostoli, Greece. In: Proceedings of the 9th Colloque National AFPS 2015, Marne-La-Vallée, France, 30 November - 2 December.

Karakostas V, Papadimitriou E, Mesimeri M, et al (2015) The 2014 Kefalonia Doublet (M6.1 and M6.0), Central Ionian Islands, Greece: seismotectonic implications along the Kefalonia transform fault zone. Acta Geophys 63:1–16. doi: 0.2478/s11600-014-0227-4

Konakli K, Der Kiureghian A, Dreger D (2014) Coherency analysis of accelerograms recorded by the UPSAR array during the 2004 Parkfield earthquake. Earthq Eng Struct Dyn 43:641–659. doi: 10.1002/eqe.2362

Louvari E, Kiratzi A, Papazachos BC (1999) The Cephalonia Transform fault and its extension to western Lefkada Island (Greece). Tectonophysics 308:223–236–223–236.

Luco J, Wong H (1986) Response of a rigid foundation to a spatially random ground motion. Earthq Eng Struct Dyn 14:891–908.

Menke W, Lerner-Lam AL, Dubendorff B, Pacheco J (1990) Polarization and coherence of 5 to 30 Hz seismic wave fields at a hard-rock site and their relevance to velocity heterogeneities in the crust. Bull Seism Soc Am 80:430–449.

Miron S, Le Bihan N, Mars J (2005) High resolution vector-sensor array processing using quaternions.

629 Miron S, Le Bihan N, Mars J (2006) Quaternion-MUSIC for vector-sensor array processing.
630 IEEE Trans Signal Process 54:1218–1229.
631 Perron V, Hollender F, Mariscal A, et al (2018) Accelerometer, velocimeter dense-array, and
632 rotation sensor datasets from the Sinaps@ post-seismic survey (Cephalonia 2014-2015
633 aftershock sequence). Seism Res Lett (in press):0–0.
634 Sbaa S, Hollender F, Perron V, et al (2017) Analysis of rotation sensor data from the Sinaps@
635 Kefalonia (Greece) post-seismic experiment — Link to surface geology and wave-field
636 characteristics. Earth, Planets Sp. doi: https://doi.org/10.1186/s40623-017-0711-6
637 Schmidt RO (1986) Multiple emitter location and signal parameter estimation. IEEE Trans
638 Antennas Propag 34:276–280–276–280.
639 Schneider JF, Stepp JC, Abrahamson NA (1992) The spatial variation of earthquake ground
640 motion and effects of local site conditions. Proc theTenth World Conf Earthq Eng Madrid,
641 Spain 2:967–972.
642 Steidl JH, Tumarkin AG, Archuleta RJ (1996) What is a reference site? Bull Seismol Soc Am
643 86:1733–1748.
644 Svay A, Perron V, Imtiaz A, et al (2017) Spatial coherency analysis of seismic ground motions
645 from a rock site dense array implemented during the Kefalonia 2014 aftershock sequence.
646 Earthq Eng Struct Dyn. doi: 10.1002/eqe.2881
647 Theodoulidis N, Cultrera G, Cornou C, et al (2017) Basin effects on ground motion: the case
648 of a high-resolution experiment in Cephalonia (Greece). Bull Earthq Eng. doi:
649 https://doi.org/10.1007/s10518-017-0225-4
650 Theodoulidis N, Karakostas C, Lekidis V, et al (2016) The Cephalonia, Greece, January 26
651 (M6.1) and February 3, 2014 (M6.0) earthquakes: near-fault ground motion and effects
652 on soil and structures. Bull Earthq Eng 14:1–18. doi: 10.1007/s10518-015-9807-1
653 Toksoz MN, Dainty AM, Charrette III EE (1991) Spatial variation of ground motion due to

654 lateral heterogeneity. Struct Saf 10:53–77.
655 Zerva A, Stephenson WR (2011) Stochastic Characteristics of Seismic Excitations at a Non-
656 Uniform (Rock and Soil) Site. Soil Dyn Earthq Eng 31:1261–1284.

LIST OF FIGURE CAPTIONS

Figure 1 : Location of the study area and the arrays. (a) The Argostoli study area in the Cephalonia Island. (b) Two arrays on the geological map of the area (Cushing et al. 2016). Layout of the (c) rock and (d) soft-soil array.

Figure 2 : Dataset recorded by the rock-site array. (a) Location of the selected events with respect to the site. The white circles show the other events recorded by the array. (b) Duration of the selected time windows for coherency analysis.

Figure 3 : EW component of the velocity time series from an earthquake (ID #11 in Table 1: M_L = 3.5, Baz= N 348, R_{epi} = 13 km, H=31 km) recorded by the stations in the array. The time window between the red lines are considered for the coherency analysis of the event.

Figure 4 : Backazimuth distribution of the dominant incoming waves from the event no. 11 (Table 1) as a function of (a) time and (b) frequency. Red line marks the event-backazimuth.

Figure 5 : Cumulative histogram of the backazimuth, extracted from the wavefield analysis of the selected dataset, considering the entire diffracted wavefield, and diffracted waves identified as Love and Rayleigh waves, respectively, for the (a)-(c) rock and (d)-(f) soft-soil array.

Figure 6 : Repartition of energy (mean ± 1σ) carried out by identified Rayleigh (R) and Love (L) waves, from the wavefield analysis of the selected dataset, considering the (a)-(b) diffracted and (c)-(d) direct waves, for the rock and soft-soil array. Here, the waves coming from the source-backazimuth ± 20° direction are represented as the direct waves and the rest are considered as the diffracted waves.

Figure 7 : Lagged coherency estimated from the EW component of velocity time series (Figure 3) of the event no. 11 recorded by the rock array. Here, coherency is presented for the pairs between the central station (B0R0 in Figure 1c) and the other stations lying along five array-branch directions at four separation distances (a) 10 m, (b) 30 m, (c) 90 m and (d) 180 m.

Figure 8 : Median ATANH coherency estimated from the (a)-(d) EW and (e)-(h) Z component of the velocity time series at four separation distances. The corresponding lagged coherency values are marked at the right-side axis. Thin grey curves represent the 'individual median' of the events recorded by the rock array and thick black curves represent their 'global median'. Red thick curves show the 'global median' estimated from the dataset recorded by the soft-soil array. The dashed curves show the respective $\pm 1\sigma$ bound of the 'global median' ATANH coherency for the two arrays. Grey horizontal lines mark the coherency resolvability threshold.

Figure 9 : EW component of the 'global median' ATANH coherency, considering only the station pairs lying along the five array-branch directions at four separation distances, from the datasets recorded by the (a)-(d) rock and (e)-(h) soft-soil arrays.

Figure 10 : Comparison of the 'global median' coherency estimated from Argostoli rock and soft-soil arrays with the existing semi-empirical ('LW 1986' for Luco and Wong 1986; 'M 1990' for Menke et al. 1990) and empirical ('A 2007' for Abrahamson 2007; 'A 2011' for Abrahamson et al. 2011) coherency models for the (a)-(d) horizontal and (e)-(h) vertical component of the ground motion at four separation distances.

AUTHORS' AFFILIATIONS, ADDRESSES

1. Afifa Imtiaz

BRGM, F-45060 Orléans, France

a.imtiaz@brgm.fr

2. V. Perron

CEA, DEN, F-13108 St Paul lez Durance Cedex, France

Univ. Grenoble Alpes, Univ. Savoie Mont-Blanc, CNRS, IRD, IFSTTAR, ISTerre, Bâtiment OSUG C, CS 40700, 38058 Grenoble Cedex 9, France

IRSN, F-92260 Fontenay-aux-Roses, France

vincent.perron.mail@gmail.com

3. F. Hollender

CEA, DEN, F-13108 St Paul lez Durance Cedex, France

fabrice.hollender@cea.fr

4. P-Y. Bard

Univ. Grenoble Alpes, Univ. Savoie Mont-Blanc, CNRS, IRD, IFSTTAR, ISTerre, Bâtiment OSUG C, CS 40700, 38058 Grenoble Cedex 9, France

pierre-yves.bard@univ-grenoble-alpes.fr

4. C. Cornou

Univ. Grenoble Alpes, Univ. Savoie Mont-Blanc, CNRS, IRD, IFSTTAR, ISTerre, Bâtiment OSUG C, CS 40700, 38058 Grenoble Cedex 9, France

cecile.cornou@univ-grenoble-alpes.fr

6. A. Svay

IMSIA, University Paris-Saclay, France

angkeara.svay@polytechnique.edu

7. N. Theodoulidis

Institute of Engineering Seismology and Earthquake Engineering (ITSAK), GR-55102 Thessaloniki, Greece

ntheo@itsak.gr

731 **TABLES**

732 Table 1: Characteristics[1] of the selected events from the rock array (Figure 1 c) data

ID	YY-MM-DD_hhmmss	PGV (m/s)	M_L	H (km)	R_{epi} (km)	Baz (N°)	Ts (s)	T (s)	Missing station(s)
1	2014-02-06_180549	1.918	3.9	8	16.3	299.9	2.21	26	-
2	2014-02-07_012153	1.134	4.2	20	104.4	80.5	6.62	50	-
3	2014-02-08_031503	2.295	3.5	18	16.4	267.7	1.79	21	-
4	2014-02-08_213038	0.038	2.4	16	36.9	268.2	2.22	42	-
5	2014-02-10_100754	0.463	2.6	17	19.0	93.9	1.9	21	-
6	2014-02-10_102933	0.043	2.5	10	48.8	240.0	1.54	31	B2R3
7	2014-02-12_221352	0.161	3.1	13	30.8	349.0	2.39	31	-
8	2014-02-13_064249	0.744	3.2	7	10.6	264.6	1.91	31	-
9	2014-02-13_171411	0.125	2.7	15	31.0	244.0	1.77	31	-
10	2014-02-14_003600	0.017	2.8	10	128.9	81.2	2.82	41	-
11	2014-02-14_012313	0.490	3.5	13	30.7	348.9	2.83	31	B2R3
12	2014-02-15_011709	0.091	2.6	3	69.0	3.5	2.87	20	B2R3
13	2014-02-16_174243	0.034	2.0	18	15.8	110.9	1.99	17	B2R3
14	2014-02-17_050452	0.104	2.4	20	40.1	230.4	1.72	32	B2R3
15	2014-02-18_045311	0.067	2.6	15	32.5	342.6	2.09	31	-
16	2014-02-18_232338	0.212	2.7	16	36.4	240.7	2.79	26	-
17	2014-02-19_130252	0.049	2.6	8	39.3	8.8	2.79	31	-
18	2014-02-20_141936	0.157	3.0	21	9.7	7.7	2.53	20	B2R4
19	2014-02-20_171321	0.020	2.4	28	169.2	134.8	5	30	-
20	2014-02-23_024435	0.017	2.1	4	64.8	6.1	4.36	31	B2R2
21	2014-02-25_045354	0.097	2.7	13	90.4	145.4	3.2	31	-
22	2014-02-25_174743	0.028	1.9	21	11.8	106.9	2.25	21	-
23	2014-02-25_175828	0.017	2.5	18	74.1	101.1	5.87	51	-
24	2014-02-25_202722	0.026	2.9	17	62.8	124.4	4.48	51	-
25	2014-02-27_142314	0.077	2.6	17	31.1	251.1	1.96	31	-
26	2014-02-27_170311	0.026	2.7	10	53.3	359.9	3.36	31	-
27	2014-02-28_221354	0.020	3.4	21	175.0	87.6	14.5	120	-
28	2014-03-01_065830	0.027	1.7	24	105.1	92.7	3.6	29	-
29	2014-03-01_132540	0.025	2.0	6	35.7	5.4	2.4	31	-
30	2014-03-02_080146	0.020	2.2	15	33.7	126.5	2.99	42	-
31	2014-03-02_194201	0.233	3.3	38	33.7	139.5	2.5	41	-
32	2014-03-03_224948	0.080	2.8	12	30.1	348.2	1.65	31	-
33	2014-03-04_171008	0.059	2.8	8	53.3	1.8	2.85	47	-
34	2014-03-05_131346	3.187	3.4	20	21.0	252.2	3.13	21	-
35	2014-03-05_155453	0.043	2.7	11	43.3	358.7	2.59	41	-
36	2014-03-06_144115	0.015	2.0	18	34.1	136.0	2.48	30	-
37	2014-03-07_174356	0.027	3.9	16	177.2	145.0	15	120	-
38	2014-03-09_035823	0.038	2.2	23	39.0	239.1	3.2	32	-
39	2014-03-09_115801	0.032	2.5	9	171.8	79.8	5.1	38	B1R4
40	2014-03-10_055054	0.033	2.0	7	27.1	10.9	2.12	21	B1R4

[1] ID is the earthquake index, YY-MM-DD_hhmmss is the date and time of the earthquake occurrence, PGV is the Peak Ground Velocity, M_L is the local magnitude, H is the hypocentral depth, R_{epi} is the epicentral distance, Baz is the earthquake backazimuth, Ts is the duration of the time window for coherency estimation and T is the signal duration for wavefield analysis.

733 Table 2: The distribution of backazimuth, epicentral distance and magnitude of the selected

734 dataset from the rock array

Backazimuth quadrant	Nb. of events	Epicentral Distance (km)	Nb. of events	Magnitude (M_L)	Nb. of events
NE	11	0-30	9	~2-3	29
NW	12	30–60	19	3–4	10
SE	10	60-100	5	4-5	1
SW	7	100–200	7		
Total	40		40		40

735

736 Table 3: Number of station pairs ideally available, when no station is missing, per event at

737 different separation distances (up to 100 m) for the rock and soft-soil arrays

Separation Distance (m)	10–20	20–30	30–40	40–50	50–60	60–70	70–80	80–90	90–100
Rock Array	19	15	16	0	7	3	2	24	15
Soft-soil Array	33	10	31	19	10	5	43	12	15

738

739 Table 4: Total number of actually available station pairs (considered for the median estimation)

740 at the selected four separation distances for the rock and soft-soil arrays.

Separation Distance (m)	10–20	20–30	30–40	80–90
Rock Array (total pairs from 40 events)	759	597	636	928
Soft-soil Array (total pairs from 46 events)	1574	414	1241	430

741

FIGURES

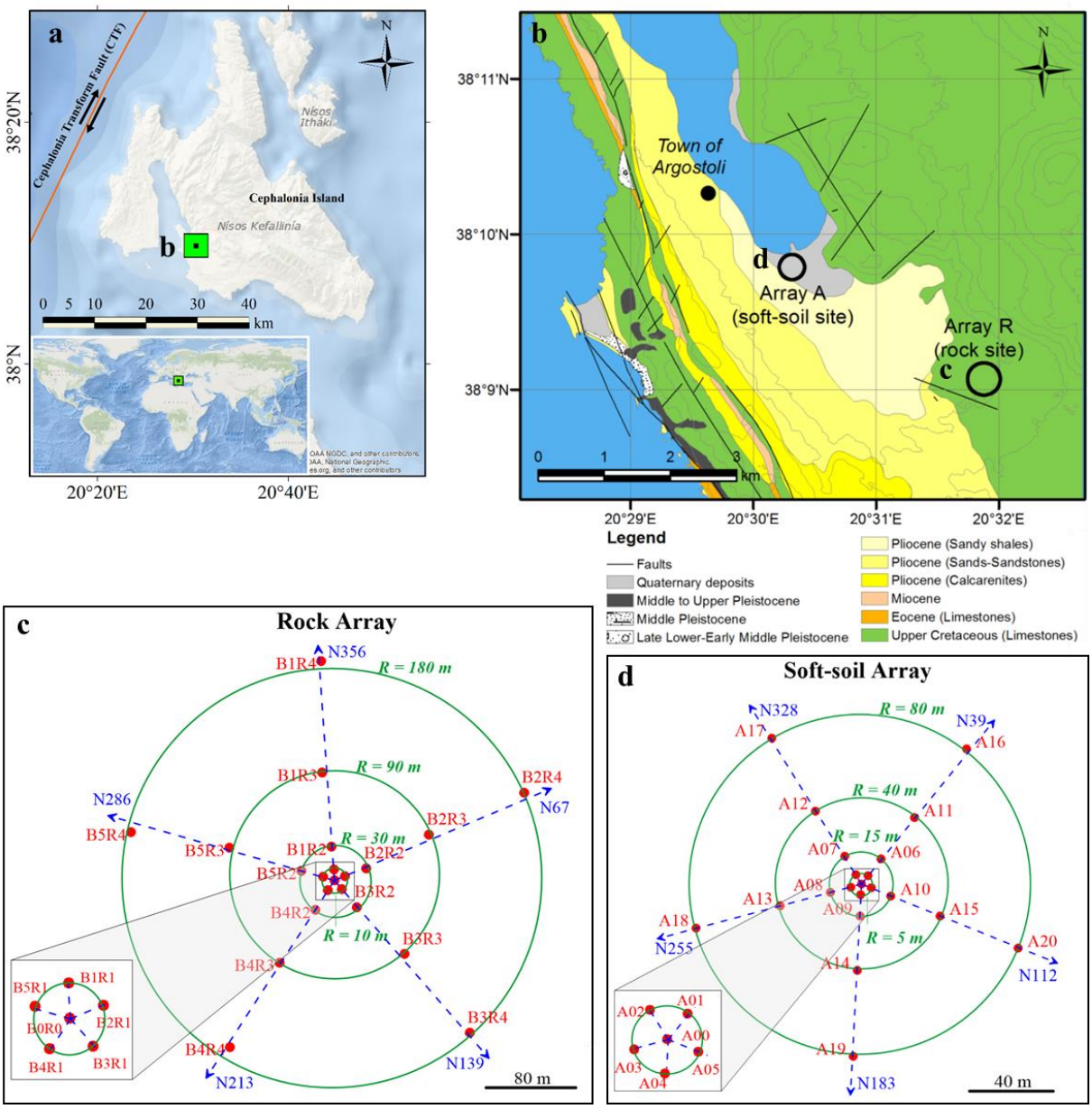


Figure 1 : Location of the study area and the arrays. (a) The Argostoli study area in the Cephalonia Island. (b) Two arrays on the geological map of the area (Cushing et al. 2016). Layout of the (c) rock and (d) soft-soil array.

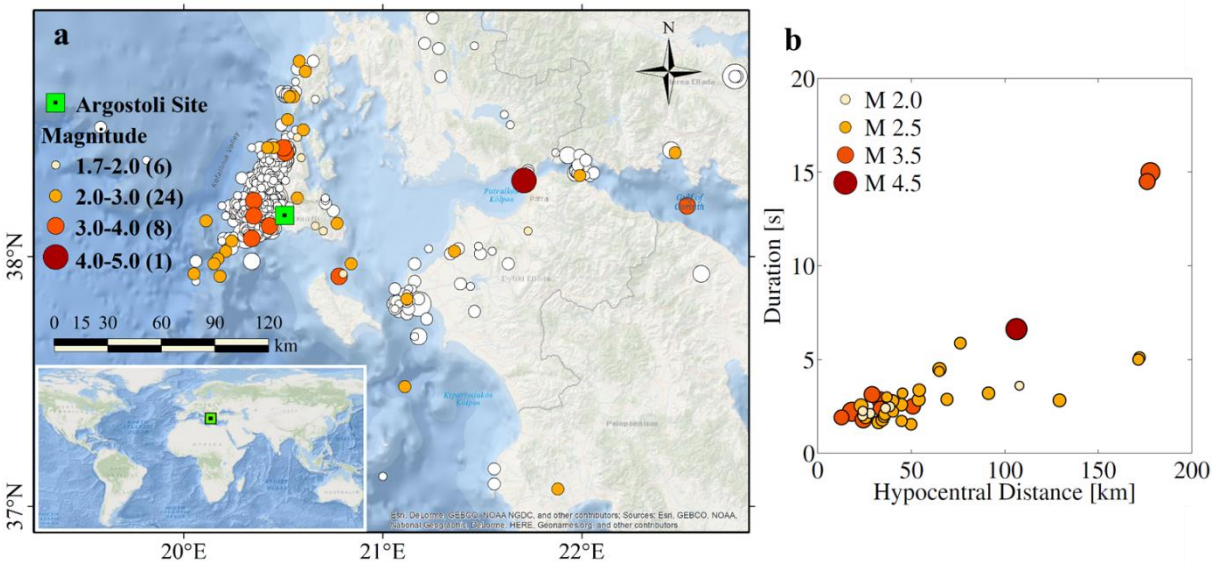


Figure 2 : Dataset recorded by the rock-site array. (a) Location of the selected events with respect to the site. The white circles show the other events recorded by the array. (b) Duration of the selected time windows for coherency analysis.

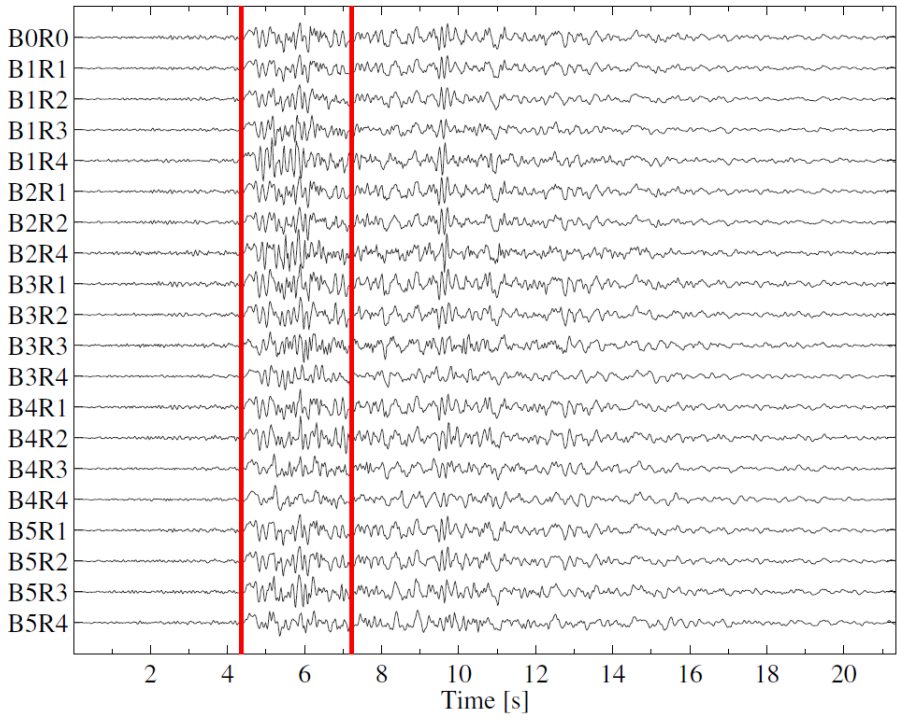


Figure 3 : EW component of the velocity time series from an earthquake (ID #11 in Table 1: M_L = 3.5, Baz= N 348, R_{epi} = 13 km, H=31 km) recorded by the stations in the array. The time window between the red lines are considered for the coherency analysis of the event.

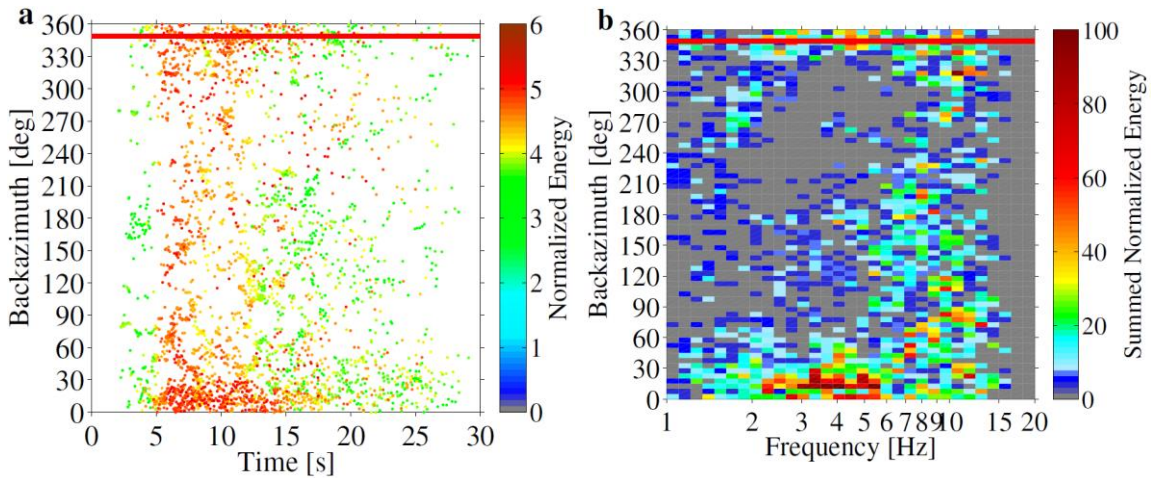


Figure 4 : Backazimuth distribution of the dominant incoming waves from the event no. 11 (Table 1) as a function of (a) time and (b) frequency. Red line marks the event-backazimuth.

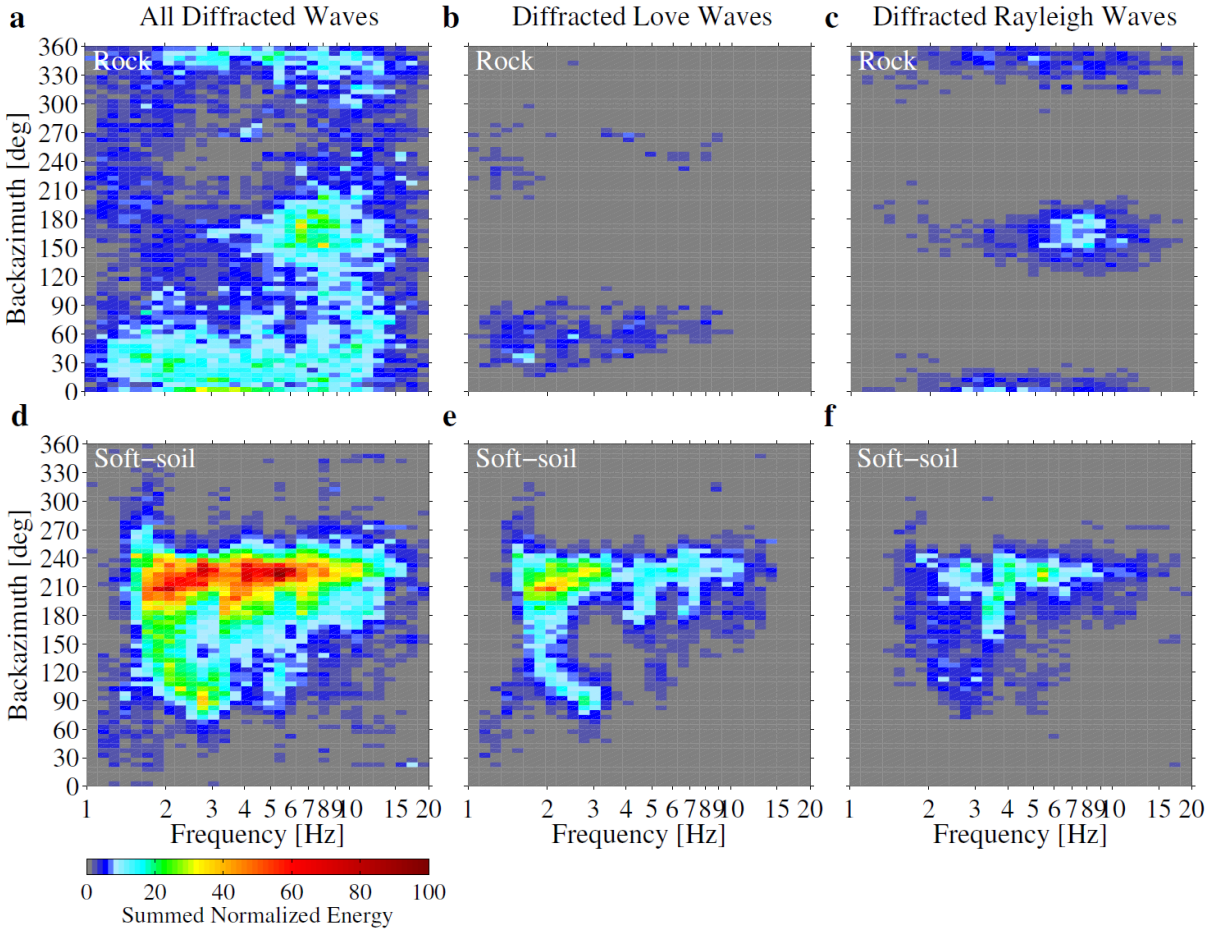


Figure 5 : Cumulative histogram of the backazimuth, extracted from the wavefield analysis of the selected dataset, considering the entire diffracted wavefield, and diffracted waves identified as Love and Rayleigh waves, respectively, for the (a)-(c) rock and (d)-(f) soft-soil array.

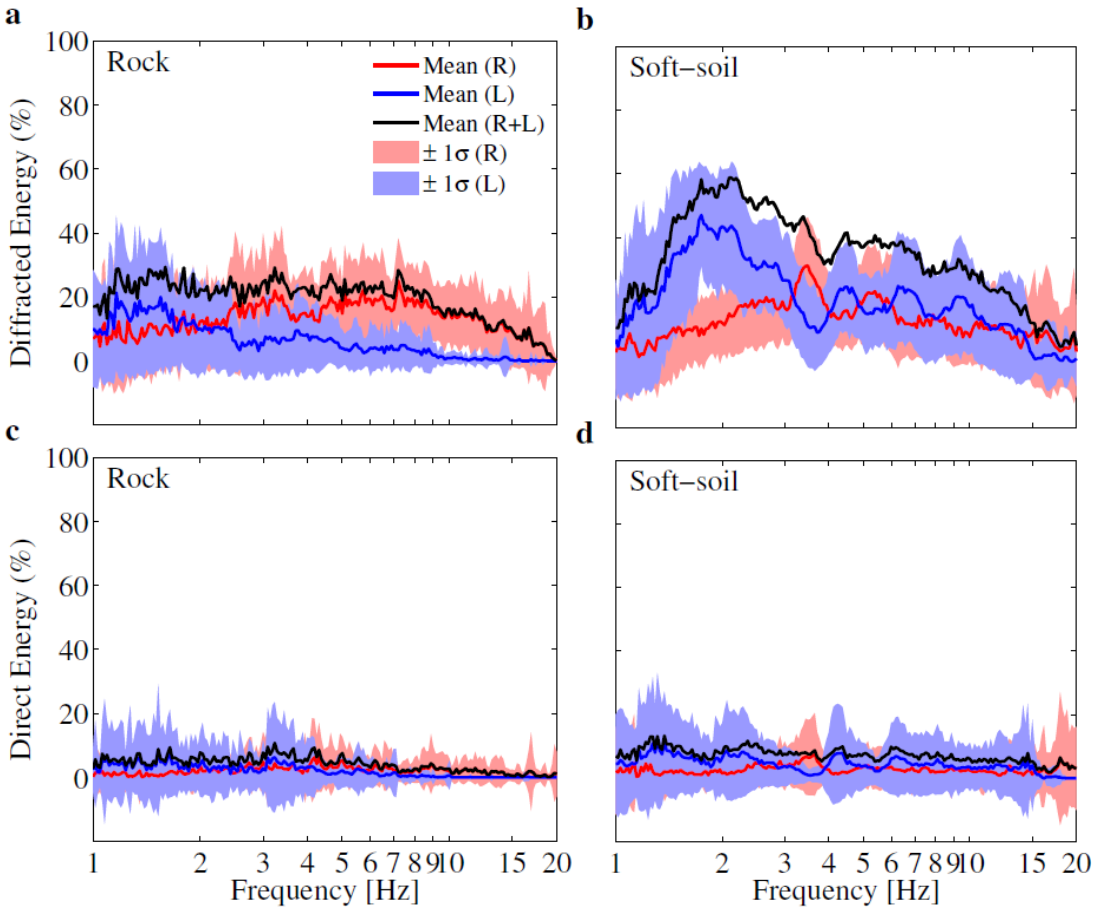


Figure 6 : Repartition of energy (mean ± 1σ) carried out by identified Rayleigh (R) and Love (L) waves, from the wavefield analysis of the selected dataset, considering the (a)-(b) diffracted and (c)-(d) direct waves, for the rock and soft-soil array. Here, the waves coming from the source-backazimuth ± 20° direction are represented as the direct waves and the rest are considered as the diffracted waves.

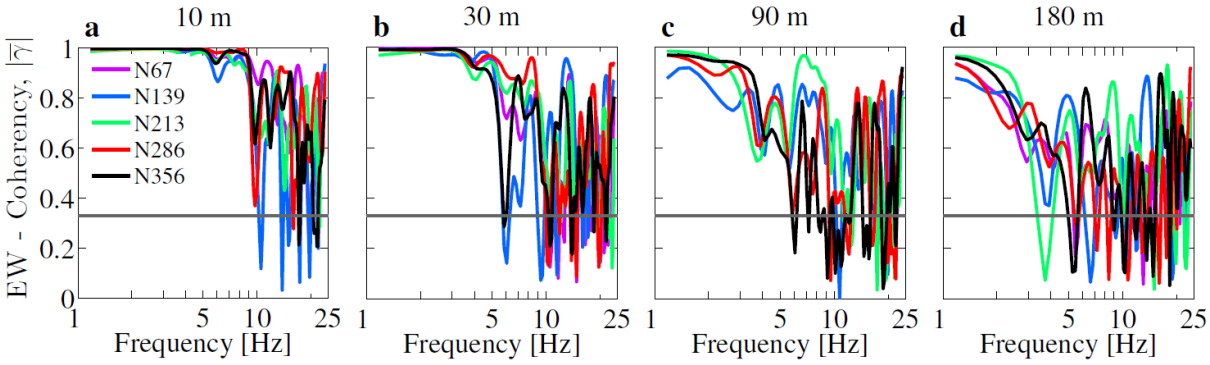


Figure 7 : Lagged coherency estimated from the EW component of velocity time series (Figure 3) of the event no. 11 recorded by the rock array. Here, coherency is presented for the pairs between the central station (B0R0 in Figure 1c) and the other stations lying along five array-branch directions at four separation distances (a) 10 m, (b) 30 m, (c) 90 m and (d) 180 m.

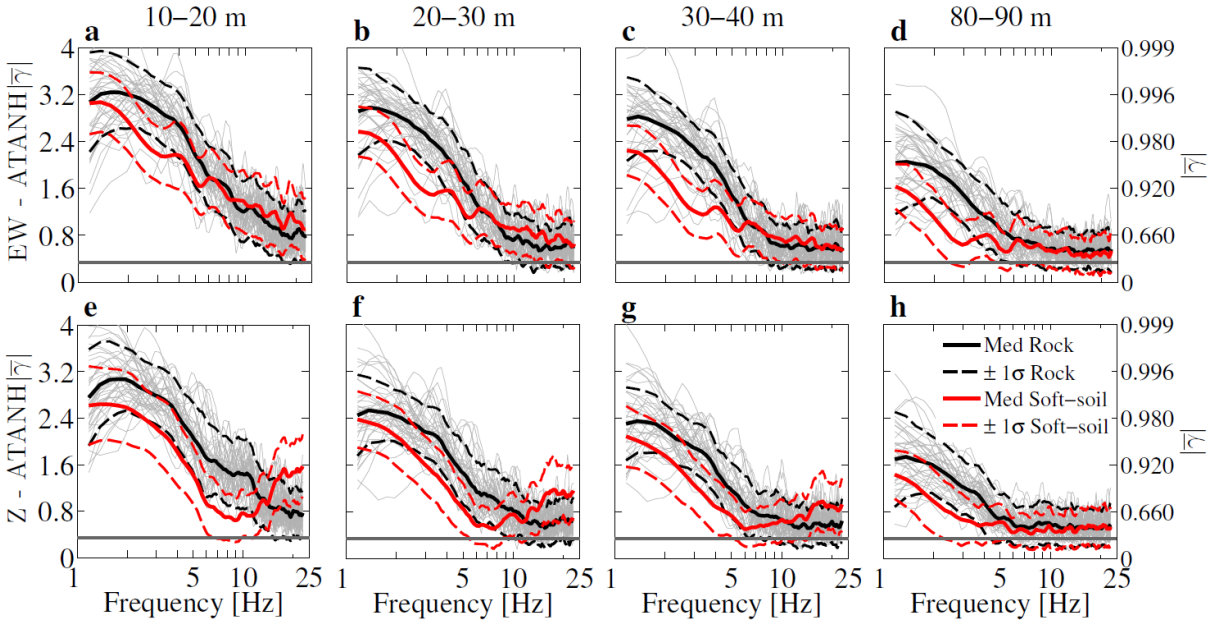


Figure 8 : Median ATANH coherency estimated from the (a)-(d) EW and (e)-(h) Z component of the velocity time series at four separation distances. The corresponding lagged coherency values are marked at the right-side axis. Thin grey curves represent the ‘individual median’ of the events recorded by the rock array and thick black curves represent their ‘global median’. Red thick curves show the ‘global median’ estimated from the dataset recorded by the soft-soil array. The dashed curves show the respective ±1σ bound of the ‘global median’ ATANH coherency for the two arrays. Grey horizontal lines mark the coherency resolvability threshold.

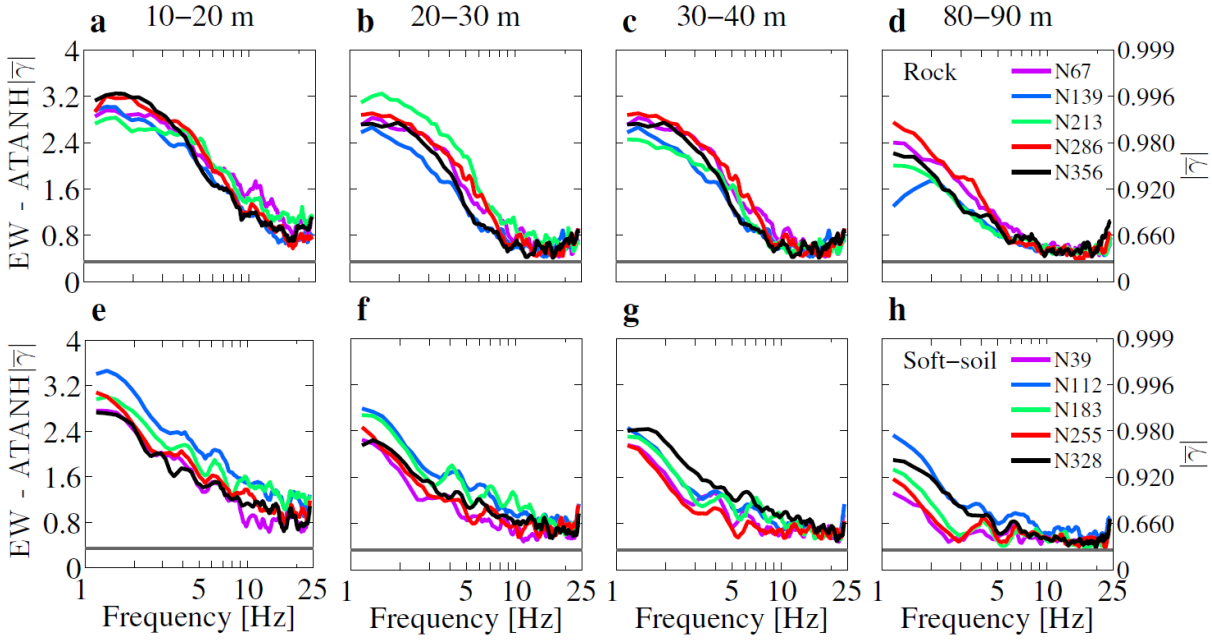


Figure 9 : EW component of the 'global median' ATANH coherency, considering only the station pairs lying along the five array-branch directions at four separation distances, from the datasets recorded by the (a)-(d) rock and (e)-(h) soft-soil arrays.

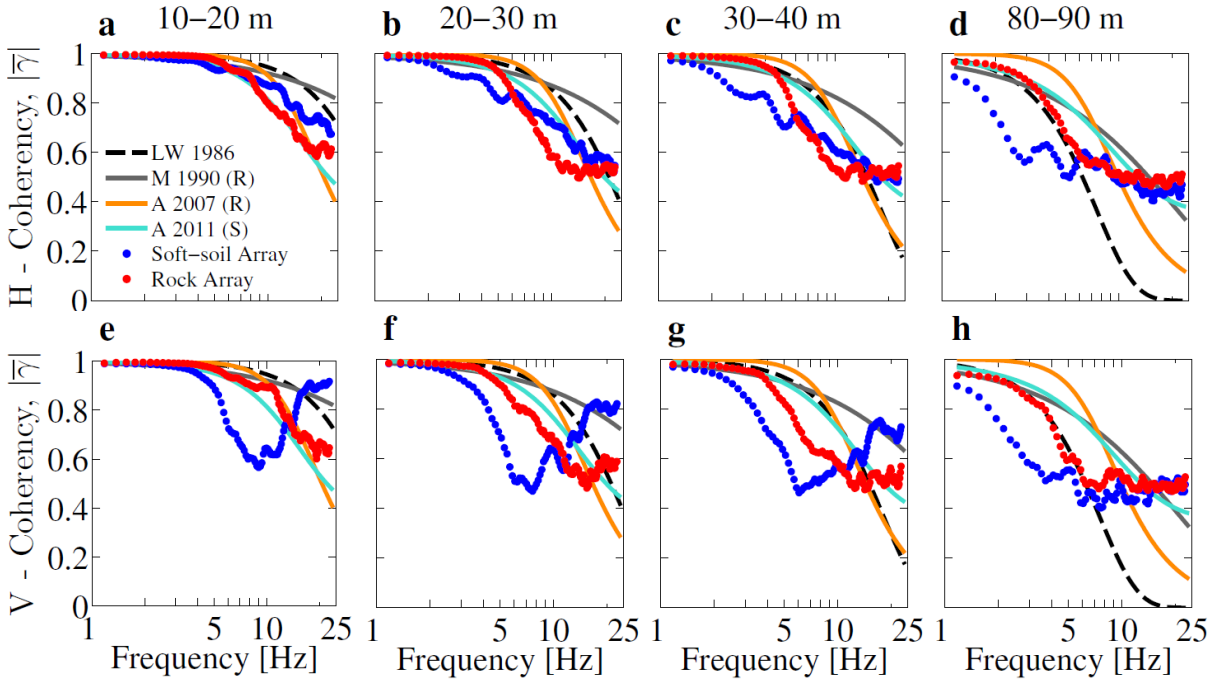


Figure 10 : Comparison of the 'global median' coherency estimated from Argostoli rock and soft-soil arrays with the existing semi-empirical ('LW 1986' for Luco and Wong 1986; 'M 1990' for Menke et al. 1990) and empirical ('A 2007' for Abrahamson 2007; 'A 2011' for Abrahamson et al. 2011) coherency models for the (a)-(d) horizontal and (e)-(h) vertical component of the ground motion at four separation distances.